Large magnetoresistance and quantum oscillations in the late transition-metal compounds T_3In_7 (T = Ni, Pd, Pt)

Joanna Blawat,[1,2,3] Przemyslaw W. Swatek,[2] Daniel Gnida,[2] Szymon Krolak,[1] Weiwei Xie,[4] Tomasz Klimczuk,[1] and Dariusz Kaczorowski[2,*]

[1]*Faculty of Applied Physics and Mathematics, Gdansk University of Technology, Narutowicza 11/12, 80-233 Gdansk, Poland*
[2]*Institute of Low Temperature and Structure Research, Polish Academy of Sciences, Ulica Okólna 2, 50-422 Wrocław, Poland*
[3]*National High Magnetic Field Laboratory, Los Alamos National Laboratory, Los Alamos, New Mexico 87545, USA*
[4]*Department of Chemistry, Michigan State University, East Lansing, Michigan 48824, USA*

(Received 17 June 2025; revised 23 September 2025; accepted 10 November 2025; published 12 December 2025)

We synthesized high-quality single crystals of T_3In_7, T = Ni, Pd, Pt, which crystallize in a body-centered-cubic *Im-3m* space group with *T*-metal-based dumbbells. The systematic study of electrical resistivity exhibits metallic behavior with extremely large nonsaturating magnetoresistance reaching 1500% at 14 T with profound Shubnikov–de Hass quantum oscillations. The fast Fourier transformation analysis shows multiple frequencies pointing to a complex structure of the Fermi surfaces. The large magnetoresistance is attributed to the presence of small, closed Fermi surfaces with light cyclotron masses with good agreement with theoretical calculations. We present the first experimental and theoretical study of the Fermi surface in the T_3In_7 family.

DOI: 10.1103/22cn-4d87

I. INTRODUCTION

Materials which exhibit extremely large magnetoresistance response have attracted a lot of attention due to the possibility of technological application as magnetic field sensors, random access memory, galvanic isolators, and spintronic devices. [1] A giant magnetoresistance effect was previously reported for many magnetic thin films [2–4] and Cr-based chalcogenide spinels [5]. Within the past few years, extreme magnetoresistance (XMR), which can reach even $\approx 10^6$%, has been discovered in many nonmagnetic compounds. Very often XMR does not saturate in high magnetic fields and might be explained by various scenarios such as classic charge carrier compensation [6], metal-insulator transition [7], and nontrivial topology of electronic bands. For example, a nonsaturating XMR effect was reported for Dirac semimetals (Cd_3As_2, ZrSiS) [8,9] and Weyl semimetals (NbP, TaAs) [10,11].

Before the discoveries of unsaturated magnetoresistance (MR) reaching 10^5% in topological semimetals, a similar characteristic was observed for $PtSn_4$, which crystallizes in a layered orthorhombic crystal structure [12]. Beyond XMR, the Shubnikov–de Haas (SdH) and de Haas-van Alpen (dHvA) effects were observed in $PtSn_4$, which allowed mapping its Fermi surface topology. Although the electronic band structure exhibits very complex band dispersions, the authors suggested that XMR in this compound cannot be attributed to electron-hole compensation [12]. Later, a Dirac node in $PtSn_4$ was discovered using angle-resolved photoemission spectroscopy (ARPES) [13]. Recently, it was suggested that the extremely high MR and the quantum oscillations in $PtSn_4$ can be explained by the existence of small Fermi surfaces with small effective masses [14]. Moreover, the Fermi surfaces are closed with equal volumes of hole and electron bands, which can explain the quadratic field dependence of MR.

Similarly, another Pt-based binary compound, Pt_3In_7, which also exhibits the Haas–van Alpen quantum oscillations, has small Fermi surfaces without open orbits, predicted by electronic band calculations [14]. The compound crystallizes with a body-centered-cubic crystal structure and belongs to a large family of materials with an Ir_3Ge_7-type structure. Many of them exhibit simple metallic behavior (for example, Ru_3Sn_7 [15]), but there are also semiconductors (such as Tc_3As_7 [16]) and a superconductor (Mo_3Sb_7 with $T_c = 2.3$ K [17]).

Up to date, very little is known about the physical properties of Pt_3In_7. Considering the similarity in Fermi surfaces between $PtSn_4$ and Pt_3In_7, and the variety of properties in the Ir_3Ge_7-type materials, we attempt to explore the electronic transport properties of Pt_3In_7. Furthermore, we study the electrical resistivity and magnetoresistance of the isostructural compounds Pd_3In_7 and Ni_3In_7. In this paper, we describe our experimental results, supported by theoretical calculations of the Fermi surfaces.

II. EXPERIMENTAL AND THEORETICAL METHODS

Single crystals of Pt_3In_7, Pd_3In_7, and Ni_3In_7 were grown using the In-flux method. The high-purity metals: Pt wire (99.9% Mennica Poland), Pd wire (99.9% Mennica Poland), Ni (99.9% Alfa Aesar), and In ingot (99.99% Alfa Aesar) were placed into alumina crucibles and sealed in quartz tubes under high vacuum. The constituents were taken in molar ratios of Pt : In, Pd : In, and Ni : In equal to 5 : 95, 10 : 90, and 2 : 98, respectively. The tube with Pt_3In_7 was heated up to 1000 °C and kept at this temperature for 12 h, then fast cooled (180 °C/h) to 600 °C and tempered for 12 h, followed by slow cooling (1 °C/h) to 300 °C. A similar process

*Contact author: d.kaczorowski@intibs.pl

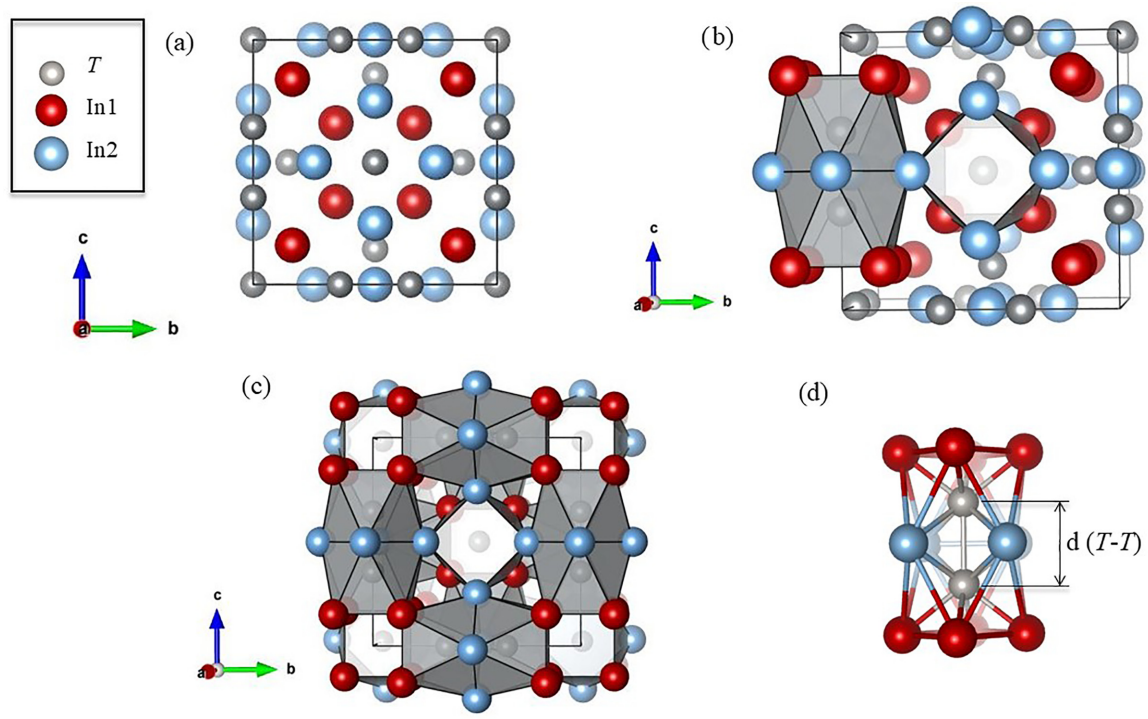

FIG. 1. Three-dimensional view of the crystal structure for T_3In_7, T = Ni, Pd, and Pt.

was performed for Ni_3In_7, but the slow-cooling step was done between 500 and 200 °C at a rate of 2 °C/h. In turn, the Pd_3In_7 sample was heated up to 950 °C and held for 12 h, followed by slow cooling at a rate of 5 °C/h to 300 °C. In each case, the remaining amount of indium flux was centrifuged at room temperature.

The chemical composition of the obtained single crystals was checked using a FEI Quanta 250FEG scanning electron microscope, equipped with an Apollo-X SDD energy-dispersive spectrometer (EDS). The energy-dispersive x-ray (EDX) spectroscopy data were analyzed using the standardless analysis in the EDAX team software. The obtained average elemental ratios were Pt : Pt : In = 29 : 71, Pd : In = 28 : 72, and Ni : In = 31 : 69, in good agreement with the expected T_3In_7 composition.

The crystal structure of the T_3In_7 crystals was examined by X-ray diffraction at room temperature on a Bruker Apex II single-crystal x-ray diffractometer with Mo Kα radiation ($\lambda = 0.71073$ Å). It was solved by direct methods and refined by the full-matrix least-squares method using SHELXL TL software [18]. The partial occupancy refinements were tested, and no vacancy or atomic mixture was discovered. The crystal structure drawings were made using VESTA software [19]. For more information, see Supplemental Material [20].

Electrical transport measurements were carried out using a Quantum Design Physical Properties Measurement System (PPMS-14). The experiments were done in the temperature range from 2 to 300 K and in magnetic fields up to 14 T employing a standard ac four-probe technique, with platinum wires attached to the specimens by silver epoxy paste.

Electronic structure calculations were performed with the all-electron general potential linearized augmented plane-wave method, as implemented in the ELK code [20]. The exchange and correlation effects were treated using the generalized gradient approximation in the form proposed by Perdew, Burke, Ernzerhof [21,22]. Strong on-site Coulomb repulsion (Hubbard U) within the fully localized limit scheme was added to d orbitals of T = Ni, Pd, and Pt [23–25]. The influence of the Coulomb repulsion on the electronic structure was tested in the range U = 2–5 eV to achieve the best agreement with the experimental quantum oscillations data. Based on this approach, the values of $U = 3.70$ eV (Pd), 3.60 eV (Pt), and 3.90 eV (Ni) were adopted, which is in line with earlier literature values reported for transition metals. The spin-orbit coupling was included as a second variational step using scalar-relativistic eigenfunctions as the basis, after the initial calculation was converged to self-consistency. The Monkhorst-Pack special k-point scheme with $8 \times 8 \times 8$ mesh was used in the first Brillouin zone sampling, and the muffin tin radius (RKmax) was set to 7.5 [26,27]. For the Fermi surface calculations and analysis, the Brillouin zone (BZ) was sampled by 32 768 k points to ensure accurate determination of the Fermi level and density. Quantum oscillation frequencies along $H \parallel [001]$ were calculated using the Supercell K-space Extremal Area Finder tool [28–30]. In the calculations, the experimental lattice parameters of Pt_3In_7, Pd_3In_7, and Ni_3In_7 were adopted.

III. RESULTS

A. Crystal structure

The analysis of single-crystal X-ray diffraction (XRD) data confirmed the successful synthesis of Pt_3In_7, Pd_3In_7, and Ni_3In_7 single crystals and thus corroborated the EDX results. The details of crystal structure refinements are gathered in

TABLE I. Single-crystal crystallographic data and structure refinement for T_3In_7, T = Ni, Pd, and Pt.

Formula	Ni_3In_7	Pd_3In_7	Pt_3In_7
F. W. (g/mol)	979.87	1122.94	1389.01
Space group, Z		*Im-3m* (#229), 4	
$a = b = c$ (Å)	9.188(2)	9.488(9)	9.432(1)
V(Å^3)	775.6(4)	854(2)	839.0(3)
Absorption correction		Numerical	
Extinction coefficient	0.0035(2)	0.0054(3)	0.0064(3)
Θ range (deg)	3.136–33.161	3.036–32.873	3.054–33.093
hkl ranges	$-10 \leqslant h \leqslant 14$	$-12 \leqslant h \leqslant 14$	$-3 \leqslant h \leqslant 14$
	$-7 \leqslant k \leqslant 12$	$-12 \leqslant k \leqslant 14$	$-12 \leqslant k \leqslant 14$
	$-3 \leqslant l \leqslant 14$	$-6 \leqslant l \leqslant 14$	$-9 \leqslant l \leqslant 13$
No. reflections, R_{int}	1794, 0.0310	3319, 0.0762	2132, 0.0362
No. independent reflections	179	191	191
No. parameters	10	10	10
R_1, wR_2 (all I)	0.0202, 0.0414	0.0209, 0.0400	0.0216, 0.0551
Goodness of fit	1.231	1.170	1.385
Largest diff. peak and hole (e^-/Å^3)	1.044, −1.219	2.783, −1.096	2.004, −1.477

Table I, and the crystallographic data are listed in Table II. All three compounds crystallize in a body-centered-cubic Ir_3Ge_7-type structure, and the lattice parameters are very similar to those reported before [31,32]. It is worth noting that for Ni_3In_7, our XRD and EDX data indicate full In atom occupancy, in contrast to the previous studies, which revealed some nonstoichiometry: $Ni_3In_{5.4}$ [33], $Ni_3In_{6.4}$ [34], and $Ni_{2.8}In_{7.2}$ [35].

The crystal structure of T_3In_7 is shown in Fig. 1. The view along the crystallographic a axis is displayed in Fig. 1(a), with one specified unique site of transition metal T (gray balls) and two inequivalent Wyckoff positions of In atoms (blue and red balls). Each T atom is surrounded by four In1 atoms and four In2 atoms, which form together a polyhedron with square antiprisms. As shown in Fig. 1(b), the fundamental unit is built from two octahedrons with the transition metal in the center and one shared antiprism. The arrangement of these blocks is presented in Fig. 1(c). Every unit is aligned along the crystallographic axis and forms two interpenetrating networks [32].

It is worth noting that the distance between T and T atoms is relatively short, i.e., d(Pt−Pt) = 2.901(9) Å, d(Pd−Pd) = 2.878(3) Å, and d(Ni−Ni) = 2.659(2) Å, which suggests that these units can be considered as dimer clusters. Each dimer is surrounded by 12 In atoms and forms T-metal-based dumbbells. The dimers are located perpendicular to each other with a distance equal to half a unit cell. Previously, the appearance of such units was linked to the observation of specific physical properties [36,37]. For example, the presence of Fe-Fe and Co-Co dumbbells in $FeGa_3$ and $CoGa_3$, respectively, was considered crucial in interpreting their electrical transport and thermodynamic behaviors. Namely, $FeGa_3$ is a rare example of a semiconducting intermetallic compound [38], while $CoGa_3$ is a good metal showing clear dHvA quantum oscillations [39]. Moreover, $FeGa_3$ is diamagnetic material, while even the small amount of Co doping (2%) changes the behavior for Curie-Weiss paramagnetic. The arrangement of Fe-Fe dumbbells in $FeGa_3$ causes the isotropic crystal structure which is in good agreement with nonanisotropic transport properties. However, the significant

TABLE II. Atomic coordinates and isotropic displacement parameters of T_3In_7, T = Ni, Pd, and Pt. U_{eq} is defined as one-third of the trace of the orthogonalized U_{ij} tensor (Å^2).

Atom	Wyckoff	Occupancy	x	y	z	U_{eq}
			Ni_3In_7			
Ni	12*e*	1	0.3553 (1)	0	0	0.0092(2)
In1	16*f*	1	0.1608(3)	0.1608(3)	0.1608(3)	0.0123(2)
In2	12*d*	1	1/4	0	1/2	0.0136(2)
			Pd_3In_7			
Pd	12*e*	1	0.3483(5)	0	0	0.0102(6)
In1	16*f*	1	0.1622(3)	0.1622 (3)	0.1622(3)	0.0105(2)
In2	12*d*	1	1/4	0	1/2	0.0131(2)
			Pt_3In_7			
Pt	12*e*	1	0.3462(4)	0	0	0.0085(2)
In1	16*f*	1	0.1628(5)	0.1628(5)	0.1628(5)	0.0108(2)
In2	12*d*	1	1/4	0	1/2	0.0128(2)

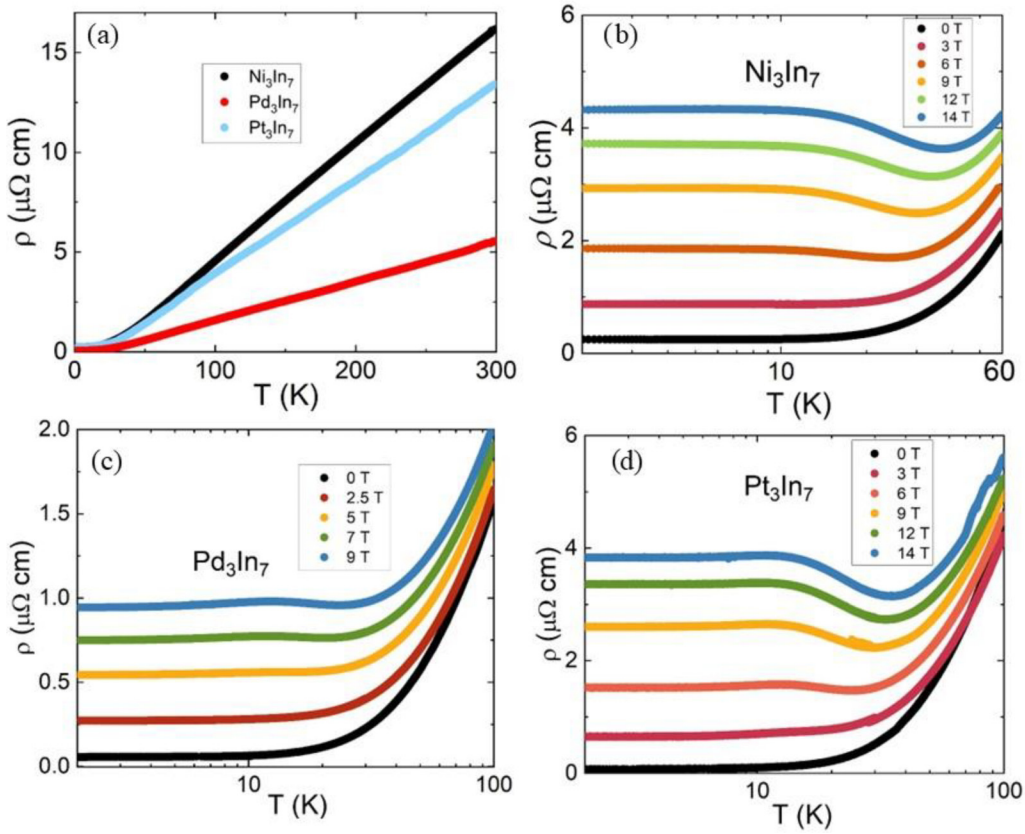

FIG. 2. (a) Temperature dependence of electrical resistivity measured in the zero magnetic field for T_3In_7, T = Ni, Pd, and Pt. Low-temperature variation of electrical resistivity measured in several magnetic fields for (b) Ni_3In_7, (c) Pd_3In_7, and (d) Pt_3In_7.

differences under Co-doping can be explained by changes in local structure. The nuclear quadrupole resonance (NQR) measurements show that in $Fe_{1-x}Co_xGa_3$, atoms prefer to form Fe-Fe or Co-Co dumbbells, but Fe-Co dumbells were also found in significant amount in the structure and could have a main influence for the structure [36,39].

B. Electrical resistivity and magnetoresistance

The temperature dependencies of the electrical resistivity of T_3In_7, T = Ni, Pd, and Pt, measured in zero magnetic field, are presented in Fig. 2(a). The compounds exhibit metallic behavior, and large values of the residual resistivity ratio RRR = R(300 K)/R(2 K), equal to 280, 100, and 64 for Pt_3In_7, Pd_3In_7, and Ni_3In_7, respectively, verifying the high quality of the single crystals examined.

As can be inferred from Figs. 2(b), 2(c), and 2(d) for Ni_3In_7, Pd_3In_7, and Pt_3In_7, respectively, in increasing transverse magnetic field, the $\rho(T)$ curves change to exhibit a broad minimum, which shifts towards higher temperatures in stronger magnetic field. Below the minimum, the resistivity increases with decreasing temperature and forms a plateau at low temperatures. The magnitude of the latter feature and turn-on region increases with increasing magnetic field. Similar behavior was observed for topologically nontrivial materials, like NbP [10], $TaSb_2$ [7], or ZrSiS [9]. However, it is also characteristic for metal-insulator transition in WTe_2 [40] or charge carrier compensation in binary rare-earth pnictides RSb and RBi [6,41–43].

The field dependencies of the transverse magnetoresistance MR = 100% × $[\rho(H) - \rho(H = 0)/\rho(H = 0)]$ of Ni_3In_7, Pd_3In_7, and Pt_3In_7 are presented in Figs. 3(a), 3(b), and 3(c), respectively. For Pt_3In_7, MR reaches 1600% at 2 K in a field of 14 T. Upon heating up to 10 K, it decreases very little; however, at higher temperatures MR drops significantly. Similar behavior was found for Pd_3In_7 and Ni_3In_7. Remarkably, for each compound, MR does not saturate in the high-field region, and clear SdH quantum oscillations are observed. While similar behavior observed for WTe_2, LuSb, LaBi, and LaSb [6,41,42,44] can be attributed to nearly perfect carrier compensation, in the case of T_3In_7 it is likely due to an uncompensated electron-hole system (see the Kohler scaling and Ref. [44]. Our theoretical calculations (see Sec. III D) show that the materials exhibit small in volume, closed Fermi pockets, which together with very low residual resistivity, and high carrier mobilities caused by a low effective mass, result in a large MR. A previously published study on Pd_3In_7 on similar crystal quality, reported linear colossal magnetoresistance (CMR) which was attributed to type II-Dirac nodes [44].

Shown in Figs. 3(d), 3(e), and 3(f) is the Kohler's scaling MR ~ $[H/\rho(H = 0)]^m$ for Ni_3In_7, Pd_3In_7, and Pt_3In_7, respectively. The best overlap of the MR isotherms was obtained with the exponent m = 1.17, 1.08, and 1.21 for Pt_3In_7, Pd_3In_7, and Ni_3In_7, respectively. The exponent m depends on the level of carriers' compensation and is expected to be equal to 2 for perfect electron-hole compensated materials, like WTe_2 [45]. The obtained values are distinctly different from m = 2;

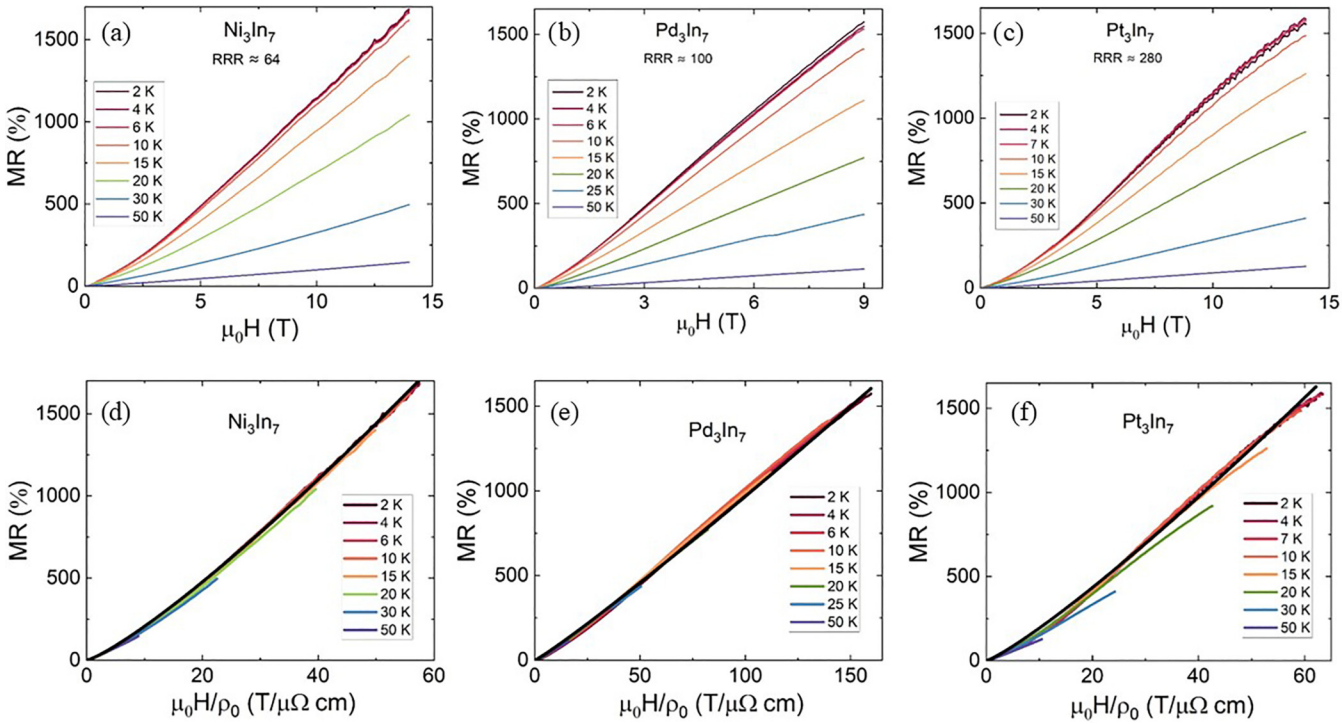

FIG. 3. Field dependence of transverse magnetoresistance measured at several temperatures for (a) Ni_3In_7, (b) Pd_3In_7, and (c) Pt_3In_7. Kohler scaling of magnetoresistance data for Ni_3In_7 (d), Pd_3In_7 (e), and Pt_3In_7 (f). Black solid line represents the fit with Kohler's equation discussed in the text.

however, similar values of m were found, e.g., for RAgSb$_2$ [44] and RSb$_2$ [46,47]. This is in agreement with the previously reported data, suggesting that Pd_3In_7 has uncompensated hole and electron pockets [44].

C. Shubnikov–de Haas oscillations

The SdH oscillations in Ni_3In_7, Pd_3In_7, and Pt_3In_7 were extracted from the experimental MR data by subtracting a higher-order polynomial. In Figs. 4(a), 4(b), and 4(c), the oscillating part of the electrical resistivity is plotted as a function of the inverse magnetic field for Ni_3In_7, Pd_3In_7, and Pt_3In_7, respectively. It is worth noting that Ni_3In_7 exhibits high-frequency oscillations, as shown in the inset to Fig. 4(a). The amplitude of the SdH oscillations decreases systematically with increasing temperature, and their shape suggests a multifrequency character, pointing to a complex structure of the Fermi surfaces (FS).

The results of FFT of the $\Delta\rho(1/H)$ data are presented in Figs. 5(a), 5(b), and 5(c) for Ni_3In_7, Pd_3In_7, and Pt_3In_7, respectively. The FFT spectrum of Ni_3In_7 shows three frequencies: $f_\alpha^{\mathrm{FFT}} = 25$ T, $f_\beta^{\mathrm{FFT}} = 138$ T, and $f_\gamma^{\mathrm{FFT}} = 3559$ T, while for Pd_3In_7 two principal frequencies were observed: $f_\alpha^{\mathrm{FFT}} = 40$ T and $f_\beta^{\mathrm{FFT}} = 109$ T. For Pt_3In_7, three principal frequencies were found, namely, $f_\alpha^{\mathrm{FFT}} = 135$ T, $f_\beta^{\mathrm{FFT}} = 161$ T, and $f_\gamma^{\mathrm{FFT}} = 490$ T. The lower frequencies may correspond to either one or two pockets of FS (see below). The other peaks in the FFT spectra can be attributed to higher harmonics. The f_β^{FFT} frequency for Pd_3In_7 and f_β^{FFT} and f_γ^{FFT} for Pt_3In_7

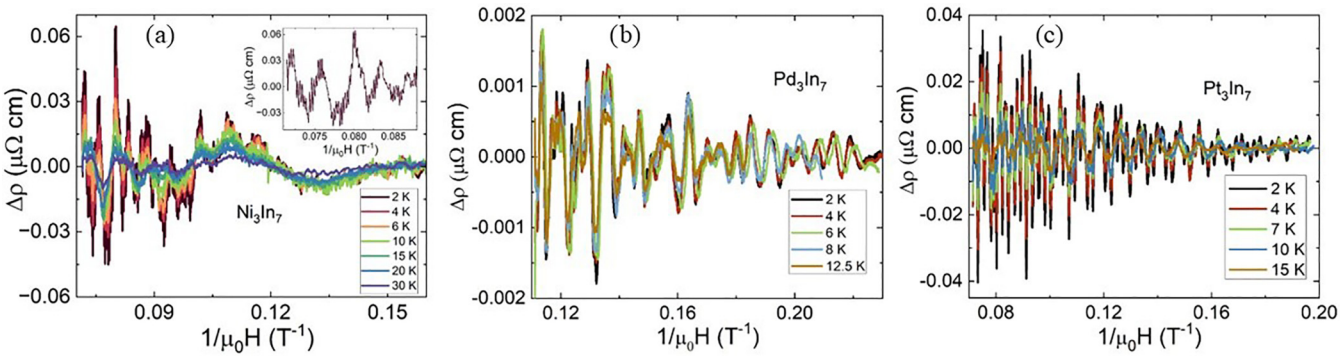

FIG. 4. Oscillating part of electrical resistivity versus inverse of magnetic field measured at a few different temperatures for (a) Ni_3In_7, (b) Pd_3In_7, and (c) Pt_3In_7. The inset shows the high magnetic field part to emphasize the high-frequency oscillations observed in Ni_3In_7.

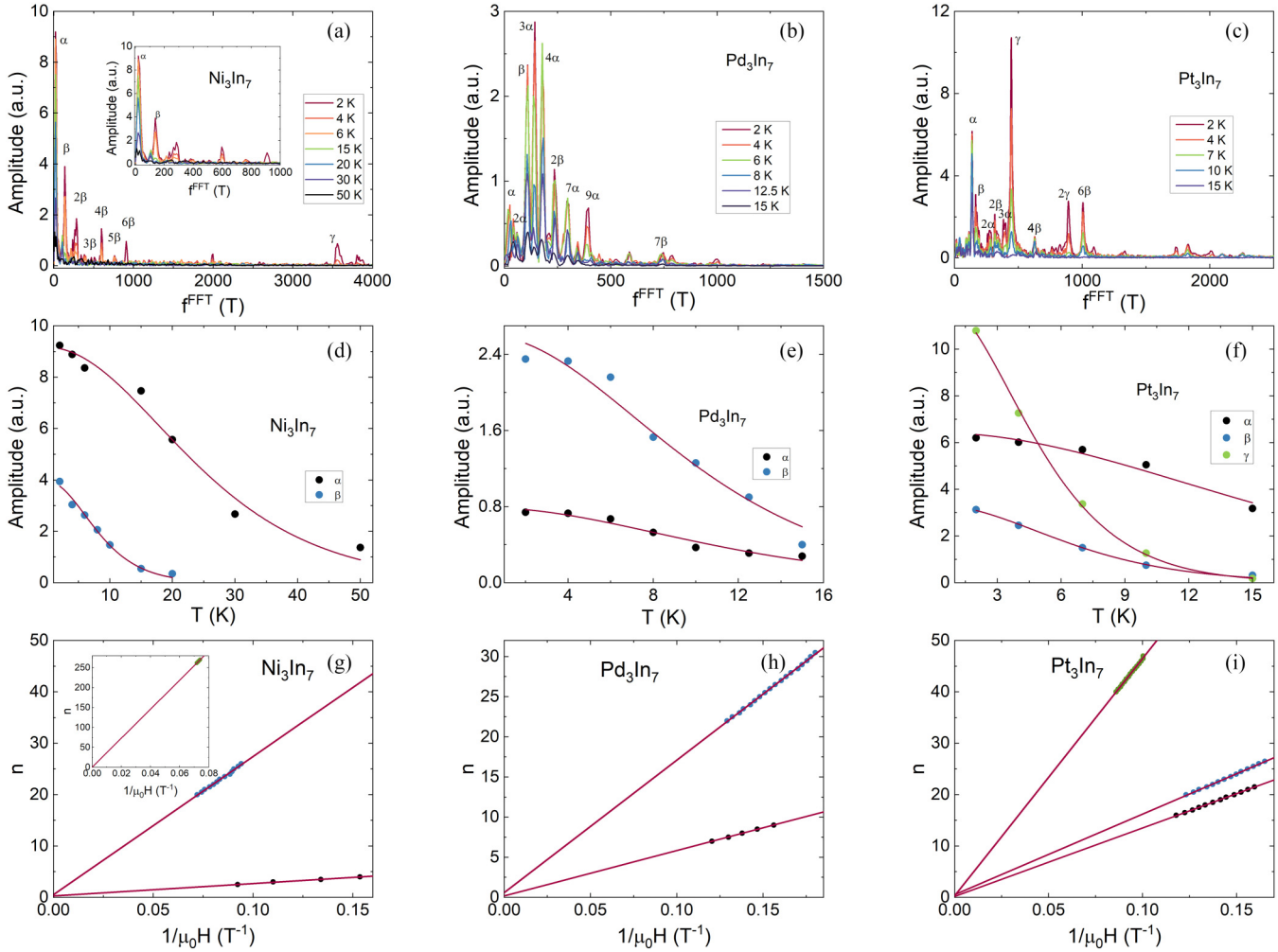

FIG. 5. Fast Fourier transform analysis of the oscillating part of the electrical resistivity data for (a) Ni_3In_7, (b) Pd_3In_7, and (c) Pt_3In_7. The temperature dependencies of the amplitudes of the principal frequencies in the FFT spectra for (d) Ni_3In_7, (e) Pd_3In_7, and (f) Pt_3In_7. The Landau fan diagram for (g) Ni_3In_7, (h) Pd_3In_7, and (i) Pt_3In_7. The solid lines represent the fit with equation discussed in the text.

were previously experimentally observed. We were able identify one lower frequency (f_α^{FFT}) for both compounds which was not observed in the reported dHvA measurements [14,44]

The temperature dependencies of the amplitudes of the peaks corresponding to the α, β, and γ pockets are shown in Figs. 5(c), 5(d), and 5(e) for Ni_3In_7, Pd_3In_7, and Pt_3In_7, respectively. The experimentally effective cyclotron masses can be calculated using the formula describing thermal damping of the SdH oscillations:

$$R_i \propto (\lambda m_i^* T B_{\mathrm{eff}})/\sinh(\lambda m_i^* T B_{\mathrm{eff}}),$$

where $B_{\mathrm{eff}} = 2/(B_1^{-1} + B_2^{-1})$ is the reciprocal of the average inverse magnetic field in the range in which the FFT analysis was performed, the constant λ can be calculated from the equation $\lambda = 2\pi^2 k_B m_0/e\hbar$ ($\sim$14.7/K), and m_i^* is the effective mass. The used values of B_{eff} are equal to 7.38 T for Pt_3In_7 and Ni_3In_7 and 5.54 T for Pd_3In_7. Applying the above formula to the experimental data [see the solid lines in Figs. 5(c)–5(e)] yielded the effective cyclotron masses: $m_\alpha^* = 0.05\ m_0$ and $m_\beta^* = 0.16 m_0$ for Ni_3In_7; $m_\alpha^* = 0.06\ m_0$ and $m_\beta^* = 0.09 m_0$ for Pd_3In_7; and $m_\alpha^* = 0.07 m_0$, $m_\beta^* = 0.17 m_0$, and $m_\gamma^* = 0.23 m_0$ for Pt_3In_7. The small effective masses are in good agreement with the previous reports on Pd_3In_7 and Pt_3In_7 [14,44].

Landau fan diagrams were constructed by assigning the maxima to integer n and the minimum to $n + 1/2$ in Figs. 5(f), 5(g), and 5(h) for Ni_3In_7, Pd_3In_7, and Pt_3In_7, respectively. The data were fitted using the Lifshitz-Onsager quantization criterion $n = F/H + \beta$, which gives $F = 838$ T and $\beta = 0.69$ below 45 T, and $F = 808$ T and $\beta = 0.65$ for the regime above 45 T. The parameter β is related to the Berry phase (ϕ_{B}) through the relation $\beta = \Phi_{\mathrm{B}}/2\pi \pm \delta$, where δ depends on the dimensionality of the Fermi surface and the curvature of the extremal orbit. For a three-dimensional band, δ is $-1/8$ for a maxima (minima) cross-section orbit on an electron (hole)-type Fermi surface, and $+1/8$ for a minima (maxima) cross-section orbit on an electron (hole) pocket. According to the theoretical calculations, the lower frequencies are associated with hole pockets (bands I–III), while the higher frequency (bands IV and V) is associated with electron pockets. The performed analysis yielded the following Berry phases: $\phi_B^\alpha = 0.37\pi$, $\phi_B^\beta = 0.81\pi$, and $\phi_B^\gamma = 0.19\pi$

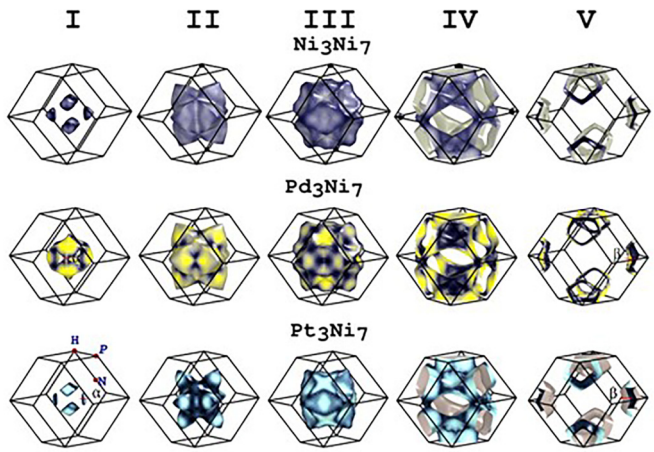

FIG. 6. Calculated Fermi surfaces of T_3In_7, T = Ni, Pd, and Pt. Greek letters mark calculated extremal orbits for the magnetic field [001] described in the text. The capital H, P, and N letters denote high-symmetry points in the Brillouin zone for reciprocal space group *Im-3m* (229).

for Ni_3In_7; $\phi_B^\alpha = 0.13\pi$ and $\phi_B^\beta = 0.95\pi$ for Pd_3In_7; and $\phi_B^\alpha = 0.15\pi$, $\phi_B^\beta = 0.81\pi$, and $\phi_B^\gamma = 0.41\pi$ for Pt_3In_7. The obtained parameters suggest a nontrivial Berry phase and can be also associated with observed large MR and small effective masses. It is worth pointing out that one pocket for Pd_3In_7 is close to π, which is in good agreement with previously reported Dirac points in that compound [44].

D. Theoretical analysis

The results of theoretical calculations are displayed in Fig. 6. For each T_3In_7 compound, five three-dimensional FS sheets typical of metals were found, three holelike and two of electronlike character. If one compares the FS sheets within each column (denoted in the figure by Roman numerals), one can easily notice that they reveal similar topological features with different transition metals T. In the first column, the compounds with Ni and Pt pose four oval-square holelike FSs along the Γ-H line with topological genus $g = 0$ [the corresponding bulk BZ along with the high-symmetry k points is shown in Fig. 6(c)]. Concurrently, in Pd_3In_7 all these pockets become clearly larger and additionally are connected by small bottlenecks around points in the middle of the Γ-N, line creating a large feature with $g = 8$ centered in the BZ. The FS sheets from column I are particularly sensitive to the value of Coulomb repulsion (Hubbard U) included in the calculations (not shown). Moreover, one can speculate that the relatively small volumes of the Fermi pockets can be also reactive to temperature changes, as was observed for WTe_2 via ARPES [48]. A corresponding topological pattern is observed in columns II and III. Rough and wrinkled structures centered at the Γ point are quite like each other with additional parts pointed out toward other high-symmetry points. In the column IV group, very complex hole FS sheets mimic the skeleton of the truncated octahedron of the BZ. In the last column, each FS sheet consists of six open spindle tori-shaped hole pockets located at point P of the edge of the BZ. Based on the overall picture of the topology of the Fermi surfaces, the qualitative analysis suggests that the large MR effect in the studied T_3In_7 compounds cannot originate from carrier compensation but should be attributed to small FS volumes and thus small effective masses of carriers.

Since the experimentally observed SdH frequencies $f_{\mathrm{Exp}}^{\mathrm{FFT}}$ are related to extremal cross-section areas A_{ex} via the Onsager relation $F = hA_{\mathrm{ex}}/2\pi e$, the theoretically calculated frequencies give the following values: 116 and 161 T (Ni_3In_7); 41, 152, and 1050 T (Pd_3In_7); and 136 and 184 T (Pt_3In_7). All calculations are done for $B \parallel [001]$. In addition to the potentially measurable frequencies for the sheets from column I, each open pocket from column V results in three further moderately low frequencies: 129, 395, and 436 T (Ni_3In_7); 108, 342, and 369 T (Pd_3In_7); and 146, 358, and 429 T (Pt_3In_7). The so-calculated frequencies that come from the Fermi surface sheets located in columns II and III are very high (in the range 3300 to 4100 T) and thus range on the edge of experimental limitation. The open pockets in Column IV can give frequencies in the range of 910–1020 T. The FFT peaks obtained experimentally in this range are very weak and barely visible [Figs. 5(a)–5(b)] and thus rather qualified as a weak component of higher harmonics of main frequencies. However, the contribution and presence of these frequencies to the resulting multifrequency FFT spectrum cannot be completely ruled out at this stage of study without comprehensive angle-resolved SdH analyses.

In contrast to the shape-sensitive properties of Fermi pockets located in column I, all the other high-frequency oscillations related to the topology of the Fermi surface sheets in columns II–V are almost nonsensitive (below 5%) to the variations of Coulomb repulsion in the range U = 1–5 eV. This behavior can indicate potentially strong localization of the filled d states in the energy space and weak d-p electron hybridization in the vicinity of the Fermi level [45]. Based on the calculations, the experimentally observed SdH frequencies $f_\alpha^{\mathrm{FFT}} = 40$ T and $f_\beta^{\mathrm{FFT}} = 109$ T for Pd_3In_7 can be assigned to two relatively small extremal orbits of the electron (column I) and hole (column V) Fermi surface pockets (41 T, $m_\alpha^{*\mathrm{calc}} = 0.09$; 108 T, $m_\beta^{*\mathrm{calc}} = 0.12$). The frequency $f_\beta^{\mathrm{FFT}} = 135$ T for Pt_3In_7 appears to be also associated with the same hole pocket (column V) located at the P point on the edge of the BZ (136 T, $m_\beta^{*\mathrm{calc}} = 0.14$). In turn, the frequency $f_\alpha^{\mathrm{FFT}} = 161$ T rather comes from the oval-square part (column I, $f = 184$ T), instead of from the bottleneck part as it is observed for Pd_3In_7. The last statement is additionally supported by the analysis of the effective cyclotron mass values ($m_\alpha^{*\mathrm{calc}} = 0.10$), which are in good agreement with the experimental data described above.

IV. CONCLUSION

In this study, we synthesized high-quality single crystals of T_3In_7, T = Ni, Pd, and Pt, which crystallize in a body-centered-cubic *Im-3m* space group. The compounds exhibit the short distance between T and T atoms and therefore the structure is formed by T-metal-based dumbbells. All compounds exhibit metallic behavior with large nonsaturating magnetoresistance reaching 1500% at 14 T. The Kohler scaling shows that the large MR is most likely not due to perfect carrier compensation. The FFT analysis of Shubnikov de Haas

quantum oscillations, together with theoretical calculations, suggests the presence of small, closed Fermi surfaces with light cyclotron masses. We presented a comprehensive magnetotransport study of this family, which will not only shed light on the behavior of these compounds but will also help in understanding the origin of large magnetoresistance.

ACKNOWLEDGMENTS

The authors thank Piotr Wisniewski and Orest Pavlosiuk for helpful discussions. P.S. is grateful to J.-P. Wang and Adam Kamiski for their invaluable insights regarding quantum oscillations. The theoretical calculations were carried out at the Wroclaw Centre for Networking and Supercomputing (WCSS) under Grant No. 359. Part of this work was performed at the National High Magnetic Field Laboratory, which is supported by National Science Foundation Cooperative Agreement No. DMR-2128556 and the State of Florida.

DATA AVAILABILITY

The data that support the findings of this article are not publicly available. The data are available from the authors upon reasonable request.

[1] J. M. Daughton, GMR applications, J. Magn. Magn. Mater. **192**, 334 (1999).

[2] G. C. Xiong, Q. Li, H. L. Ju, S. N. Mao, L. Senapati, X. X. Xi, R. L. Greene, and T. Venkatesan, Giant magnetoresistance in epitaxial $Nd_{0.7}Sr_{0.3}MnO_{3-\delta}$ thin films, Appl. Phys. Lett. **66**, 1427 (1995).

[3] M. N. Baibich, J. M. Broto, A. Fert, F. Nguyen Van Dau, F. Petroff, P. Etienne, G. Creuzet, A. Friederich, and J. Chazelas, Giant magnetoresistance of (001)Fe/(001)Cr magnetic superlattices, Phys. Rev. Lett. **61**, 2472 (1988).

[4] A. E. Berkowitz, J. R. Mitchell, M. J. Carey, A. P. Young, S. Zhang, F. E. Spada, F. T. Parker, A. Hutten, and G. Thomas, Giant magnetoresistance in heterogeneous Cu-Co alloys, Phys. Rev. Lett. **68**, 3745 (1992).

[5] A. P. Ramirez, R. J. Cava, and J. Krajewski, Colossal magnetoresistance in Cr-based chalcogenide spinels, Nature (London) **386**, 156 (1997).

[6] L.-K. Zeng *et al.*, Compensated semimetal LaSb with unsaturated magnetoresistance, Phys. Rev. Lett. **117**, 127204 (2016).

[7] Y. Li, L. Li, J. Wang, T. Wang, X. Xu, C. Xi, C. Cao, and J. Dai, Resistivity plateau and negative magnetoresistance in the topological semimetal $TaSb_2$, Phys. Rev. B **94**, 121115(R) (2016).

[8] T. Liang, Q. Gibson, M. N. Ali, M. Liu, R. J. Cava, and N. P. Ong, Ultrahigh mobility and giant magnetoresistance in the Dirac semimetal Cd_3As_2, Nat. Mater. **14**, 280 (2015).

[9] R. Singha, A. K. Pariari, B. Satpati, and P. Mandal, Large nonsaturating magnetoresistance and signature of nondegenerate Dirac nodes in ZrSiS, Proc. Natl. Acad. Sci. USA **114**, 2468 (2017).

[10] C. Shekhar *et al.*, Extremely large magnetoresistance and ultrahigh mobility in the topological Weyl semimetal candidate NbP, Nat. Phys. **11**, 645 (2015).

[11] X. Huang *et al.*, Observation of the chiral-anomaly-induced negative magnetoresistance in 3D Weyl semimetal TaAs, Phys. Rev. X **5**, 031023 (2015).

[12] E. Mun, H. Ko, G. J. Miller, G. D. Samolyuk, S. L. Bud'ko, and P. C. Canfield, Magnetic field effects on transport properties of $PtSn_4$, Phys. Rev. B **85**, 035135 (2012).

[13] Y. Wu, L.-L. Wang, E. Mun, D. D. Johnson, D. Mou, L. Huang, Y. Lee, S. L. Bud'ko, P. C. Canfield, and A. Kaminski, Dirac node arcs in $PtSn_4$, Nat. Phys. **12**, 667 (2016).

[14] T. Yara, M. Kakihana, K. Nishimura, M. Hedo, T. Nakama, Y. Ōnuki, and H. Harima, Small Fermi surfaces of $PtSn_4$ and Pt_3In_7, Phys. B Condens. Matter **536**, 625 (2018).

[15] B. C. Chakoumakos and D. Mandrus, Ru_3Sn_7 with the Ir_3Ge_7 structure-type, J. Alloys Compd. **281**, 157 (1998).

[16] F. Hulliger, New T_3B_7 Compounds, Nature (London) **209**, 500 (1966).

[17] Z. Bukowski, D. Badurski, J. Stępień-Damm, and R. Troć, Single crystal growth and superconductivity of Mo_3Sb_7, Solid State Commun. **123**, 283 (2002).

[18] G. M. Sheldrick, Crystal structure refinement with *SHELXL*, Acta Crystallogr. Sect. C: Struct. Chem. **71**, 3 (2015).

[19] K. Momma and F. Izumi, *VESTA 3* for three-dimensional visualization of crystal, volumetric and morphology data, J. Appl. Crystallogr. **44**, 1272 (2011).

[20] See Supplemental Material at http://link.aps.org/supplemental/10.1103/22cn-4d87 for additional EDX and XRD data.

[21] D. J. Singh and L. Nordstrom, *Planewaves, Pseudopotentials, and the LAPW Method* (Springer Science & Business Media, New York, 2006).

[22] J. P. Perdew, K. Burke, and M. Ernzerhof, Generalized gradient approximation made simple, Phys. Rev. Lett. **77**, 3865 (1996).

[23] A. G. Petukhov, I. I. Mazin, L. Chioncel, and A. I. Lichtenstein, Correlated metals and the LDA + U method, Phys. Rev. B **67**, 153106 (2003).

[24] A. I. Liechtenstein, V. I. Anisimov, and J. Zaanen, Density-functional theory and strong interactions: Orbital ordering in Mott-Hubbard insulators, Phys. Rev. B **52**, R5467(R) (1995).

[25] A. B. Shick, A. I. Liechtenstein, and W. E. Pickett, Implementation of the LDA+U method using the full-potential linearized augmented plane-wave basis, Phys. Rev. B **60**, 10763 (1999).

[26] F. Bultmark, F. Cricchio, O. Grånäs, and L. Nordström, Multipole decomposition of LDA + U energy and its application to actinide compounds, Phys. Rev. B **80**, 035121 (2009).

[27] P. Stoeckl, P. Swatek, and J.-P. Wang, Magnetocrystalline anisotropy of α''-$Fe_{16}N_2$ under various DFT approaches, AIP Adv. **11**, 015039 (2021).

[28] H. J. Monkhorst and J. D. Pack, Special points for Brillouin-zone integrations, Phys. Rev. B **13**, 5188 (1976).

[29] A. Kokalj, Computer graphics and graphical user interfaces as tools in simulations of matter at the atomic scale, Comput. Mater. Sci. **28**, 155 (2003).

[30] T. Björkman, CIF2Cell: Generating geometries for elec-

tronic structure programs, Comput. Phys. Commun. **182**, 1183 (2011).

[31] P. M. C. Rourke and S. R. Julian, Numerical extraction of de Haas–van Alphen frequencies from calculated band energies, Comput. Phys. Commun. **183**, 324 (2012).

[32] H. A. Friedrich and J. Köhler, Refinement of the crystal structure of triplatinum heptaindium, Pt_3In_7, Z. Kristallogr. - New Cryst. Struct. **217**, 24 (2002).

[33] U. Häussermann, M. Elding-Pontén, C. Svensson, and S. Lidin, Compounds with the Ir_3Ge_7 structure type: Interpenetrating frameworks with flexible bonding properties, Chem. - Eur. J. **4**, 1007 (1998).

[34] R. W. Cahn, Binary alloy phase diagrams, Adv. Mater. **3**, 628 (1991).

[35] E. Hellner, Das system nickel-indium, Int. J. Mater. Res. **41**, 401 (1950).

[36] M. F. Singleton and P. Nash, The In−Ni (indium-nickel) system, Bull. Alloy Phase Diagrams **9**, 592 (1988).

[37] A. S. Botana, Y. Quan, and W. E. Pickett, Disturbing the dimers: Electron and hole doping in the intermetallic insulator $FeGa_3$, Phys. Rev. B **92**, 155134 (2015).

[38] F. R. Wagner, R. Cardoso-Gil, B. Boucher, M. Wagner-Reetz, J. Sichelschmidt, P. Gille, M. Baenitz, and Y. Grin, On Fe–Fe dumbbells in the ideal and real structures of $FeGa_3$, Inorg. Chem. **57**, 12908 (2018).

[39] Y. Hadano, S. Narazu, M. A. Avila, T. Onimaru, and T. Takabatake, Thermoelectric and magnetic properties of a narrow-gap semiconductor $FeGa_3$, J. Phys. Soc. Jpn. **78**, 013702 (2008).

[40] Y. Zhao, H. Liu, J. Yan, W. An, J. Liu, X. Zhang, H. Wang, Y. Liu, H. Jiang, Q. Li, Y. Wang, X.-Z. Li, D. Mandrus, X. C. Xie, M. Pan, and J. Wang, Anisotropic magnetotransport and exotic longitudinal linear magnetoresistance in WTe_2 crystals, Phys. Rev. B **92**, 041104(R) (2015).

[41] O. Pavlosiuk, M. Kleinert, P. Swatek, D. Kaczorowski, and P. Wiśniewski, Fermi surface topology and magnetotransport in semimetallic LuSb, Sci. Rep. **7**, 12822 (2017).

[42] O. Pavlosiuk, P. Swatek, D. Kaczorowski, and P. Wiśniewski, Magnetoresistance in LuBi and YBi semimetals due to nearly perfect carrier compensation, Phys. Rev. B **97**, 235132 (2018).

[43] S. Sun, Q. Wang, P.-J. Guo, K. Liu, and H. Lei, Large magnetoresistance in LaBi: Origin of field-induced resistivity upturn and plateau in compensated semimetals, New J. Phys. **18**, 082002 (2016).

[44] Y. L. Wang, L. R. Thoutam, Z. L. Xiao, J. Hu, S. Das, Z. Q. Mao, J. Wei, R. Divan, A. Luican-Mayer, G. W. Crabtree, and W. K. Kwok, Origin of the turn-on temperature behavior in WTe_2, Phys. Rev. B **92**, 180402(R) (2015).

[45] A. Flessa Savvidou, A. Ptok, G. Sharma, B. Casas, J. K. Clark, V. M. Li, M. Shatruk, S. Tewari, and L. Balicas, Anisotropic positive linear and sub-linear magnetoresistivity in the cubic type-II Dirac metal Pd_3In_7, npj Quantum Mater. **8**, 68 (2023).

[46] K. D. Myers, S. L. Bud'ko, I. R. Fisher, Z. Islam, H. Kleinke, A. H. Lacerda, and P. C. Canfield, Systematic study of anisotropic transport and magnetic properties of $RAgSb_2$ (R = Y, La–Nd, Sm, Gd–Tm), J. Magn. Magn. Mater. **205**, 27 (1999).

[47] S. L. Bud'ko, P. C. Canfield, C. H. Mielke, and A. H. Lacerda, Anisotropic magnetic properties of light rare-earth diantimonides, Phys. Rev. B **57**, 13624 (1998).

[48] A. Teruya, M. Takeda, A. Nakamura, H. Harima, Y. Haga, K. Uchima, M. Hedo, T. Nakama, and Y. Ōnuki, Characteristic Fermi surface properties of V_2Ga_5, $CoGa_3$, $TiGa_3$, $ZrGa_3$, and $ZrAl_3$ with different tetragonal structures, J. Phys. Soc. Jpn. **84**, 054703 (2015).